

# ADMap: Anti-disturbance framework for reconstructing online vectorized HD map

Haotian Hu  
Leapmotor

hu\_haotian@leapmotor.com

Laifeng Hu  
Leapmotor

hu\_laifeng@leapmotor.com

Fanyi Wang  
Zhejiang university

11730038@zju.edu.cn

Jingwei Xu  
Leapmotor

xu\_jingwei@leapmotor.com

Yaonong Wang  
Leapmotor

wang\_yaonong@leapmotor.com

Zhiwang Zhang  
NingboTech University

zhiwang.zhang@nit.zju.edu.cn

## Abstract

In the field of autonomous driving, online high-definition (HD) map reconstruction is crucial for planning tasks. Recent research has developed several high-performance HD map reconstruction models to meet this necessity. However, the point sequences within the instance vectors may be jittery or jagged due to prediction bias, which can impact subsequent tasks. Therefore, this paper proposes the Anti-disturbance Map reconstruction framework (ADMap). To mitigate point-order jitter, the framework consists of three modules: Multi-Scale Perception Neck, Instance Interactive Attention (IIA), and Vector Direction Difference Loss (VDDL). By exploring the point-order relationships between and within instances in a cascading manner, the model can monitor the point-order prediction process more effectively. ADMap achieves state-of-the-art performance on the nuScenes and Argoverse2 datasets. Extensive results demonstrate its ability to produce stable and reliable map elements in complex and changing driving scenarios. Code and more demos are available at <https://github.com/hht1996ok/ADMap>.

## 1. Introduction

In the field of autonomous driving, HD map reconstruction is a crucial task. This process involves converting the sensor-collected information into instance-level vector representations, such as lane lines, road boundaries, and pedestrian crossings. These representations enable the vehicle to capture detailed road topology and ground semantics information while driving, which can be effectively applied to downstream regulation tasks. In recent years, high-definition maps have grown significantly. Early work

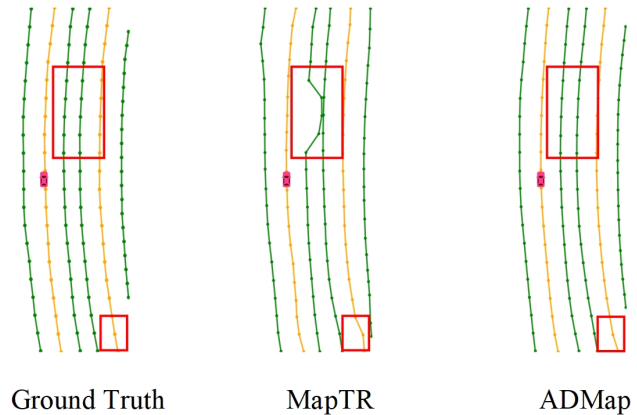


Figure 1. Visual comparison between ADMap and baseline, ADMap effectively mitigates the point-order jitter problem.

[3, 21, 8, 10] predicted dense ground information, which resulted in redundancy in model computation and annotation. HDMaNet [9] groups dense pixel segmentation results into sparse vectorized instances, but this requires a complex post-processing process. VectorMapNet [14] predicts vectorized instances for the first time, using an autoregressive decoder to predict the instance points in an ordered manner. MapTR [12] predicts vectorised instances end-to-end and resolves feature ambiguities caused by different point order directions effectively. MapTRv2 [13] adds decoupled self-attention to capture intra-instance point relations in parallel.

As shown in Fig. 1, we observe that the predicted points in the instances tend to be inevitably jittered or shifted, causing the reconstructed instance vectors to become distorted or jagged, which seriously affects the quality and utility of the online high-precision maps.

The incomplete interaction between instance points and map topological information leads to inaccurate point prediction in existing models. This is due to the models not fully considering inter- and intra-instance interactions. Furthermore, using L1 loss alone for distance supervision does not effectively utilize the geometric relationship between point sequences to constrain the prediction process. To address this, the network must utilize the characteristics of the vector line segments between points to more finely constrain the position of the point sequences.

To address this issue, we propose the Anti-Disturbance Map reconstruction framework (ADMap). ADMap utilises Multi-Scale Perception Neck (MPN), Instance Interactive Attention (IIA) and Vector Direction Difference Loss (VDDL) to more accurately predict point-order topology.

MPN enables the network to capture multi-scale features in the BEV map, improving the accuracy of reconstructing instances with significant size differences in the scene without increasing inference time. IIA flexibly encodes instance-level and point-level information, feature interactions between instance embeddings further help the network capture the relationships between point-level embeddings, and more accurate point-level information makes the reconstruction more accurate. VDDL models the association between instance points and vector direction differences, and uses vector direction differences as losses to constrain the reconstruction process of point sequences more precisely. Additionally, the difference in real vector direction is utilised to assign varying weights to the points in the instances, ensuring that the model can more effectively capture the rapidly changing map information in the scene.

We validate the effectiveness of ADMap in nuScenes and Argoverse2. ADMap achieves leading performance in both nuScenes and Argoverse2 compared to existing reconstructed vectorized high-precision map models. In nuScenes, ADMap improved performance by 3.9% and 5.4% in camera-only and multimodal frameworks, respectively, compared to the baseline. ADMapv2 not only reduced inference latency but also improved baseline performance. ADMap also performed well in Argoverse2. ADMapv2 improves mAP by 68.7% while FPS maintaining 13.9, demonstrating that ADMap is an efficient and high-precision framework for generating accurate and smooth map topology in complex scenes.

Contributions of this paper are summarized as follows:

- End-to-end ADMap is proposed, which reconstructs more stable vectorized HD maps.
- MPN captures multi-scale information more precisely without increasing computational resources, IIA achieves effective interaction between inter-instance and intra-instance information to alleviate the problem of instance point position offset. VDDL models the

vector direction difference and supervises the reconstruction process of point order position using topological information.

- ADMap enables real-time reconstruction of vectorized HD maps and achieves top performance in both the nuScenes and Argoverse2 benchmarks.

## 2. Related Work

### 2.1. Lane detection

In previous research, lane line detection was typically considered a standalone task. Information was gathered through sensors such as cameras and lidar to identify and locate lane lines. LaneNet [16] proposes a semantic segmentation of 2D lane lines and clusters them. 3D-LaneNet [5] is a pioneering work in the field of monocular 3D lane lines, which proposes a new type of dual-path structure that implements Inverse Perspective Mapping (IPM) projection of features inside the network. GenLaneNet [6] optimizes the anchor representation of 3D-LaneNet and uses the anchor to predict 3D Lane in a more reliable coordinate system. PersFormer [2] proposes a unified framework for 2D and 3D lane detection. The framework introduces transformer into the spatial transformation module to improve the robustness of features.

### 2.2. HD map reconstruction

Traditional online local maps[3, 21, 8, 10, 15, 11, 17] are mostly based on semantic segmentation of multiple perspective views, which are converted to bird’s eye view (BEV) using IPM projection and splicing, and then go through a complicated post-processing to get the map elements. HDMapNet [9] reconstructs the HD map from the generated semantic segmentation results, instance embedding, and direction prediction. However, it requires complicated post-processing and has low accuracy. VectorMapNet [14] achieves end-to-end HD map reconstruction by aligning the reconstruction task with the target detection paradigm and generating ordered point sets one by one through Polyline Generator. MapTR [12] generates map elements directly using the Deformable DETR-based object detection paradigm. It introduces permutation-equivalent in the model to address the order uniqueness constraints during point-order matching.

ADMap utilizes features between instance embeddings to model the relationships between point-level embeddings. Also, the introduction of vectorial direction differences also supervises the point order position more finely.

### 3. Method

#### 3.1. Overview

As shown in Figure 2, ADMap takes both a multiview image and a point cloud as inputs. The image features of the multi-view image  $I = \{I_1, \dots, I_M\}$  are extracted using the 2D backbone. The 2D image is then converted to a BEV perspective by LSS-Base view transformer to obtain camera BEV features  $F_{cam} \in R^{H \times W \times C}$ . The point cloud  $P \in R^{n \times C}$  is voxelized and placed into a 3D backbone to obtain lidar BEV features  $F_{lidar} \in R^{H \times W \times C}$ . Fusion Layers fuses camera BEV features and lidar BEV features into fusion BEV features  $F_{fusion} \in R^{H \times W \times C}$ . These features are then input into the Multi-Scale Perception Neck (Section 3.2), which fuses the multi-scale BEV features from top to bottom. This ensures that the network can accurately predict instances of different scales in the scene. We follow the network structure of the transformer decoder in MapTR [12], with the difference that we additionally add Instance Interactive Attention (Section 3.3) to the decoder, which helps the network to better capture the associations between point levels through the extracted instance embeddings. Furthermore, the details of Vector Direction Difference Loss are presented in Section 3.4.

#### 3.2. Multi-Scale Perception Neck

Conventional FPN structures only output fused multi-scale features, which prevents the network from delicately capturing information at all levels of scale. To make more detailed BEV features available to the network, we propose Multi-Scale Perception Neck (MPN), whose inputs are fusion BEV features  $F_{fusion} \in R^{H \times W \times C}$ . After downsampling, each layer of BEV features will be connected to an upsampling layer to restore the feature map to its original size. The final feature map of each layer will be merged into a multi-scale BEV feature  $F_{mc} \in R^{H \times W \times C}$ . Figure 2 shows that the dotted line indicates that the step is only implemented during training, while the solid line indicates that the step is implemented during both training and inference. During training, the multi-scale BEV features and the BEV feature maps at each level are fed into the transformer decoder, which allows the network to predict the instance information of the scene in different scales. During the inference process, MPN only outputs multi-scale BEV features  $F_{mc} \in R^{H \times W \times C}$  and not the feature maps at each level, which ensures that the model inference speed remains constant.

#### 3.3. Transformer Decoder

A set of instance-level queries  $q_{ins} \in R^{N_i \times C}$  and a set of point-level queries  $q_{pos} \in R^{N_p \times C}$  are defined in the Transformer Decoder, and we subsequently share the point-level queries across all instances, and these hierarchical queries  $q$

are defined as:

$$q = q_{ins} + q_{pos} \quad (1)$$

The decoder contains several cascading decoding layers that iteratively update the hierarchical queries. In each decoding layer, the hierarchical queries are fed into self-attention, which allows the hierarchical queries to exchange information with each other. Deformable Attention is used to facilitate interaction between the hierarchical queries and the multiscale BEV features  $F_{mc} \in R^{H \times W \times C}$ .

##### 3.3.1 Instance Interactive Attention

In order to better acquire the features of each instance in the decoding stage, we propose Instance Interactive Attention (IIA). IIA comprises Instance self-attention and Point self-attention. Unlike the parallel extraction of instance-level and point-level embeddings[13], our IIA cascades to extract point-order embeddings, feature interactions between instance embeddings assist the network in learning the topological relationships between instance points.

Figure 3 shows that the hierarchical embedding  $F_{hie} \in R^{(N_i * N_p) \times C}$  produced by Deformable cross-attention is inputted into Instance self-attention. After merging the point dimension with the channel dimension, the dimension transformation of the hierarchical embedding is  $F_{hie} \in R^{N_i \times (C * N_p)}$ . Subsequently, the hierarchical embedding is put into an embed layer consisting of multiple MLPs to obtain the instance query, which is put into multi-head self-attention to capture the topological relations among instances. The instance embedding  $F_{ins} \in R^{N_i \times C}$  is obtained. To include instance-level information in the point-level embedding, we add the instance embedding  $F_{ins} \in R^{(N_i * 1) \times C}$  to the hierarchical embedding  $F_{hie} \in R^{(N_i * N_p) \times C}$ . The summed features are fed into the value Point self-attention, which interacts with the points within each instance to further finely correlate the topological relationships between point sequences.

##### 3.3.2 Vector Direction Difference Loss

HD maps contain vectorized static map elements, including lane lines, road edges, and pedestrian crossings. We propose Vector Direction Difference Loss (VDDL) for these open shapes (lane lines, road edges) and closed shapes (crosswalks). By modeling the point-order vector direction inside the instance, the difference between the predicted vector direction and the real vector direction is used for finer supervision of the point-order position. In addition, points with large differences in the direction of the ground truth are thought to represent drastic changes in the topological outcome of the scene (more difficult to predict), and are given more attention by more models. To ensure accurate prediction of drastically varying points, the network

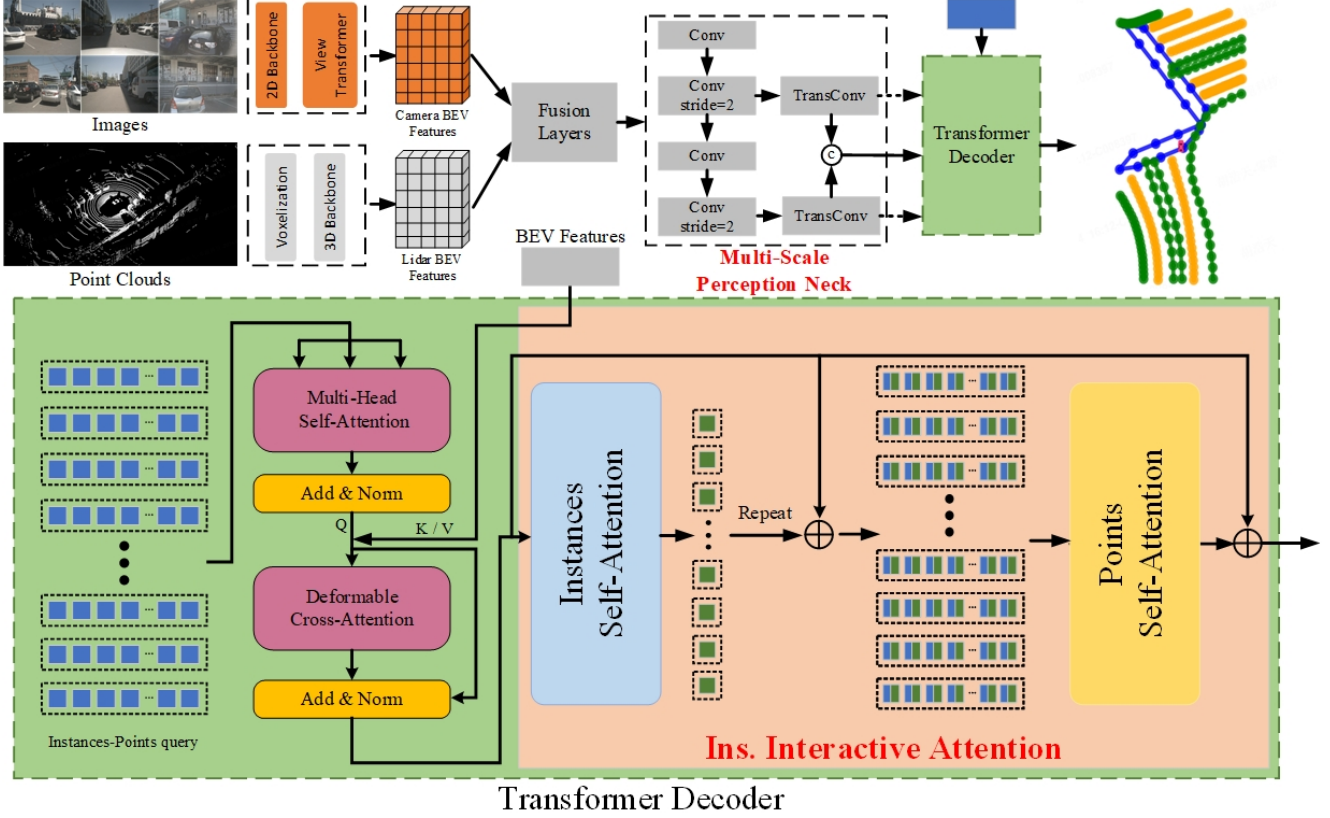


Figure 2. Schematic diagram of the overall framework of ADMMap. The figure displays the MPN and IIA proposed in this paper. The process is performed only during training when indicated by the dashed line, and during both training and inference when indicated by the solid line. Several hierarchical query are defined in the decoder to represent the topology of the map, and self-attention and cross-attention are used to interact with the BEV map. Instance self-attention and Points self-attention further interact with inter- and intra-instance information.

assigns greater weight to points with a large difference in the direction of the real vector.

Figure 4 illustrates the modeling of the predicted vector line  $\{L_{i,j}^{pre}\}_{i=0,j=0}^{N_i,N_p-1}$  and the real vector line  $\{L_{i,j}^{gt}\}_{i=0,j=0}^{N_i,N_p-1}$  in the predicted point sequence  $\{P_{i,j}^{pre}\}_{i=0,j=0}^{N_i,N_p}$  and the real point sequence  $\{P_{i,j}^{gt}\}_{i=0,j=0}^{N_i,N_p}$ .

To ensure that the loss value increases with the angular difference, we compute the vector line angle difference cosine  $\cos\theta_{i,j}^{pre}$ :

$$\cos\theta_{i,j}^{pre} = \begin{cases} \frac{\text{sum}(L_{i,j}^{pre} * L_{i,j}^{gt})}{\text{norm}(L_{i,j}^{pre}) * \text{norm}(L_{i,j}^{gt})}, & j \neq N_p, \\ 0, & j = N_p, \end{cases} \quad (2)$$

The sum function accumulates the 2D coordinate positions of the vector lines, while the norm function normalizes them. We assign weights of different magnitudes to the vector angular differences of the points in the real example.

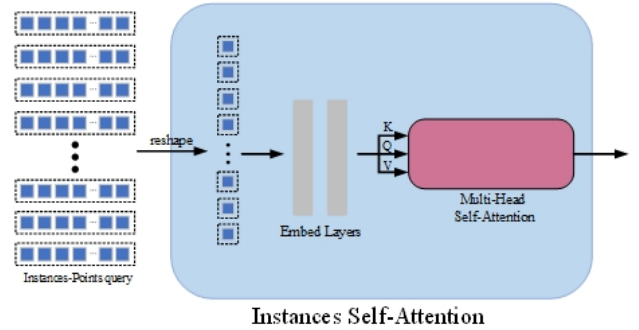


Figure 3. Schematic diagram of Instance self-attention. The point and channel dimensions in the hierarchical query are merged and put into embedded layers consisting of multiple MLPs to compress the dimensions. These query are then used in multi-head self-attention for instance-level interactions.

The weights  $W_{i,j}^{vec}$  are defined as follows:

$$\cos\theta_{i,j}^{gt} = \begin{cases} \frac{\text{sum}(L_{i,j-1}^{gt} * L_{i,j}^{gt})}{\text{norm}(L_{i,j-1}^{gt}) * \text{norm}(L_{i,j}^{gt})}, & j \neq N_p \\ 0, & j = 0 \text{ or } N_p, \end{cases} \quad (3)$$

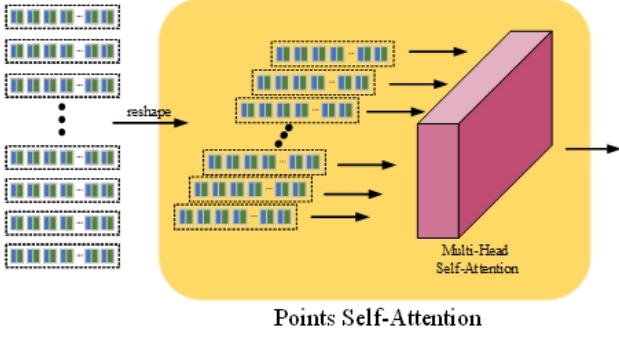


Figure 4. Schematic of points self-attention. It groups the output query of instance self-attention so that each instance is fed into multi-head self-attention separately for point-level interaction.

$$W_{i,j}^{vec} = \begin{cases} \exp\left(\frac{1.0 - \cos\theta_{i,j}^{gt}}{2}\right), & i \neq 0 \text{ and } i \neq N_p \\ 1.0, & i = 0 \text{ or } i = N_p, \end{cases} \quad (4)$$

where  $N_p$  represents the number of points in the instance, and  $\exp()$  represents an exponential function with base  $e$ . The weight of the first and last points is set to 1 since they cannot compute the vector angular difference. When the vector angular difference in the ground truth becomes larger, we assign a larger weight to the point, which makes the network more attentive to significantly varying map topology. The Vector Direction Difference Loss  $L_{i,j}^{vec}$  is:

$$L_{i,j}^{vec} = \sum_{i=0}^{N_i} \sum_{j=0}^{N_p-1} (1 - \cos\theta_{i,j}^{pre}) * W_{i,j}^{vec} + \sum_{i=0}^{N_i} \sum_{j=1}^{N_p} (1 - \cos\theta_{i,j}^{pre}) * W_{i,j}^{vec} \quad (5)$$

We use  $1 - \cos\theta$  to adjust the interval of loss by  $[0, 2]$ . By summing the cosines of the angle differences of neighboring vector lines at each point, the loss captures more comprehensive information about the geometric topology of each point. The loss at the first and last points is the cosine of the angular difference between the unique neighboring vectors.

## 4. Experiments

### 4.1. Dataset and metric

The effectiveness of ADMap was verified in nuScenes [1] and Argoverse2 [19] datasets. The nuScenes dataset includes 40,000 labeled data with keyframes sampled at 2 HZ. It consists of 6 surround view cameras and 1 lidar with a FOV of 360 degrees. Argoverse2 contains 1000 labeled multi-modal data sequences, which contains high resolution

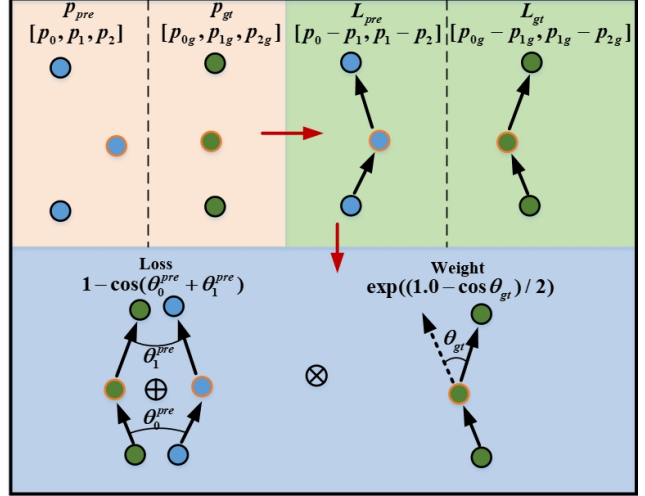


Figure 5. Flowchart of Vector Direction Difference Loss. The point sequence  $P$  is modeled as a vector line  $L$  and the vector direction difference between the predicted and ground truth is calculated. The weights of each instance point are obtained from the geometric topological relations of ground truth.

images from 7 surround view cameras and 2 stereo cameras, in addition to lidar point clouds and attitude aligned maps, etc. To ensure a fair evaluation of ADMap, we classify the map elements into three categories: lane lines, road boundaries and pedestrian crossings. We use Average Precision (AP) to evaluate the quality of the map construction, and using the sum of the chamfer distances of the predicted and real point sequences to determine whether they match or not. Chamfer distance thresholds are set to  $[0.5, 1.0, 1.5]$ , and we separately under these three thresholds calculate the AP and take the average as the metric.

### 4.2. Detail

ADMap is trained using 8\* NVIDIA Geforce RTX A100 GPUs. The batch size is set to 8, the learning rate is set to  $6e-4$ , and the AdamW optimizer as well as the cosine annealing schedule are used. The point cloud range is set to  $[-15.0, -30.0, -5.0, 15.0, 30.0, 3.0]$ , and the voxel size is set to  $[0.15, 0.15, 0.2]$ . We use ResNet50 [7] as the camera backbone and SECOND [20] as the lidar backbone. The number of input channels of MPN is 256 and the number of output channels is  $[512, 512, 512]$ . In the loss function, the weights of L1 Loss and VDDL are set to 5.0 and 1.0, respectively.

### 4.3. Comparative experiment

#### 4.3.1 nuScenes

Table 1 reports the metrics of ADMap and the state-of-the-art methods on the nuScenes dataset. It is evident that ADMap outperforms the baseline in both camera-only and

Table 1. Results of ADMap in nuScenes benchmark compared to each state-of-the-art method. We performs validation in both camera-only and multimodal frameworks with 24 and 110 training epochs, respectively. ADMap uses MapTR as the baseline, while ADMapv2 uses MapTRv2 as the baseline. FPS is measured on NVIDIA RTX 3090 GPU with batch size of 1. 'C' denotes the use of camera, and 'L' denotes the use of lidar. Bolding indicates best performance.

Model	Modality	Backbone	Epoch	$AP_{div}$	$AP_{ped}$	$AP_{bou}$	mAP	FPS
HMapNet [9]	C	EB0	30	27.7	10.3	45.2	27.7	0.9
HMapNet [9]	C & L	EB0 & PP	30	16.3	29.6	46.7	31.0	0.5
VectorMapNet [14]	C	R50	110	42.5	51.4	44.1	46.0	2.2
VectorMapNet [14]	C & L	R50 & PP	110	48.2	60.1	53.0	53.7	-
PivotNet [4]	C	R50	24	56.2	56.5	60.1	57.6	6.7
BeMapNet [18]	C	R50	30	62.3	57.7	59.4	59.8	4.2
MapTR [12]	C	R50	24	51.5	46.3	53.1	50.3	15.1
MapTR [12]	C & L	R50 & SEC	24	55.9	62.3	69.3	62.5	6.0
ADMap	C	R50	24	56.2	49.4	57.9	54.5	14.8
ADMap	C & L	R50 & SEC	24	66.6	63.3	74.0	68.0	5.8
ADMap	C & L	R50 & SEC	110	66.5	71.2	76.9	71.5	5.8
MapTRv2 [13]	C & L	R50 & SEC	24	65.6	66.5	74.8	69.0	5.8
ADMapv2	C & L	R50 & SEC	24	67.9	68.5	74.5	70.3	6.1
<b>ADMapv2</b>	<b>C &amp; L</b>	<b>R50 &amp; SEC</b>	<b>110</b>	<b>67.7</b>	<b>73.8</b>	<b>76.6</b>	<b>72.7</b>	<b>6.1</b>

Table 2. Results of ADMap in Argoverse2 benchmark compared to each state-of-the-art method. ADMap uses MapTR as the baseline, while ADMapv2 uses MapTRv2 as the baseline. FPS is measured on NVIDIA RTX3090 GPU with batch size of 1. 'C' denotes the use of camera, and 'L' denotes the use of lidar. \* indicates the replicated results in the same framework.

Model	Modality	Backbone	Epoch	$AP_{div}$	$AP_{ped}$	$AP_{bou}$	mAP	FPS
HMapNet [9]	C	EB0	-	13.1	5.7	37.6	18.8	-
VectorMapNet [14]	C	R50	-	38.3	36.1	39.2	37.9	-
MapTR* [12]	C	R50	6	65.5	56.6	61.8	61.3	14.8
ADMap	C	R50	6	68.9	60.3	64.9	64.7	14.2
ADMap	C & L	R50 & SEC	6	75.5	69.5	80.5	75.2	9.3
MapTRv2 [13]	C	R50	6	62.9	72.1	67.1	67.4	12.0
ADMapv2	C	R50	6	72.4	64.5	68.9	68.7	13.9
<b>ADMapv2</b>	<b>C &amp; L</b>	<b>R50 &amp; SEC</b>	<b>6</b>	<b>76.2</b>	<b>72.8</b>	<b>81.5</b>	<b>76.9</b>	<b>8.9</b>

multimodal frameworks. In the camera-only framework, ADMap improves 4.2% compared to MapTR. In the multimodal framework, ADMap improves by 5.5% compared to MapTR and ADMapv2 improves by 1.3% compared to MapTRv2, with a maximum accuracy of 72.7%, which achieves the best performance in this benchmark.

In terms of speed, both ADMap and ADMapv2 demonstrate excellent performance. ADMap significantly improves model performance compared to the baseline, with only a slight decrease in FPS of 0.3 and 0.2. It is worth noting that ADMapv2 not only improves performance but also enhances inference speed compared to the baseline. The inference latency of the multimodal framework is reduced from 172.4ms to 163.9ms.

### 4.3.2 Argoverse2

Table 2 reports the metrics of ADMap and the state-of-the-art methods on the Argoverse2 dataset. In the camera-only framework, ADMap and ADMapv2 improved by 3.4% and 1.3% compared to the baseline, respectively. In the multimodal framework, ADMap and ADMapv2 achieved the

best performance in the benchmark with 75.2% and 76.9%. Regarding inference speed, the latency of ADMapv2 decreased by 11.4ms compared to MapTRv2.

### 4.4. Ablation experiment

Table 3 shows the results of the ablation experiments for each module in the nusenes benchmark. On the basis of MapTR, we added three modules, MPN, IIA and VDDL. The results indicate that mAP increased by 2.9% after adding IIA, 1.9% after adding MPN, and 0.7% after adding VDDL.

Table 4 compares the effect of adding a self-attention to enhance the baseline. The results show that IIA achieves the best performance, improving by 1.3% compared to Decoupled self-attention [13].

Table 5 shows how the performance is affected by adding backbone and neck. The mAP increased by 1.2% with the addition of the backbone and neck of SECOND[20], and the model mAP increased by 2.0% with the addition of MPN, without increasing the inference time.

Table 6 shows the impact of the VDDL weights on the performance of the nuScenes benchmark. The best perfor-

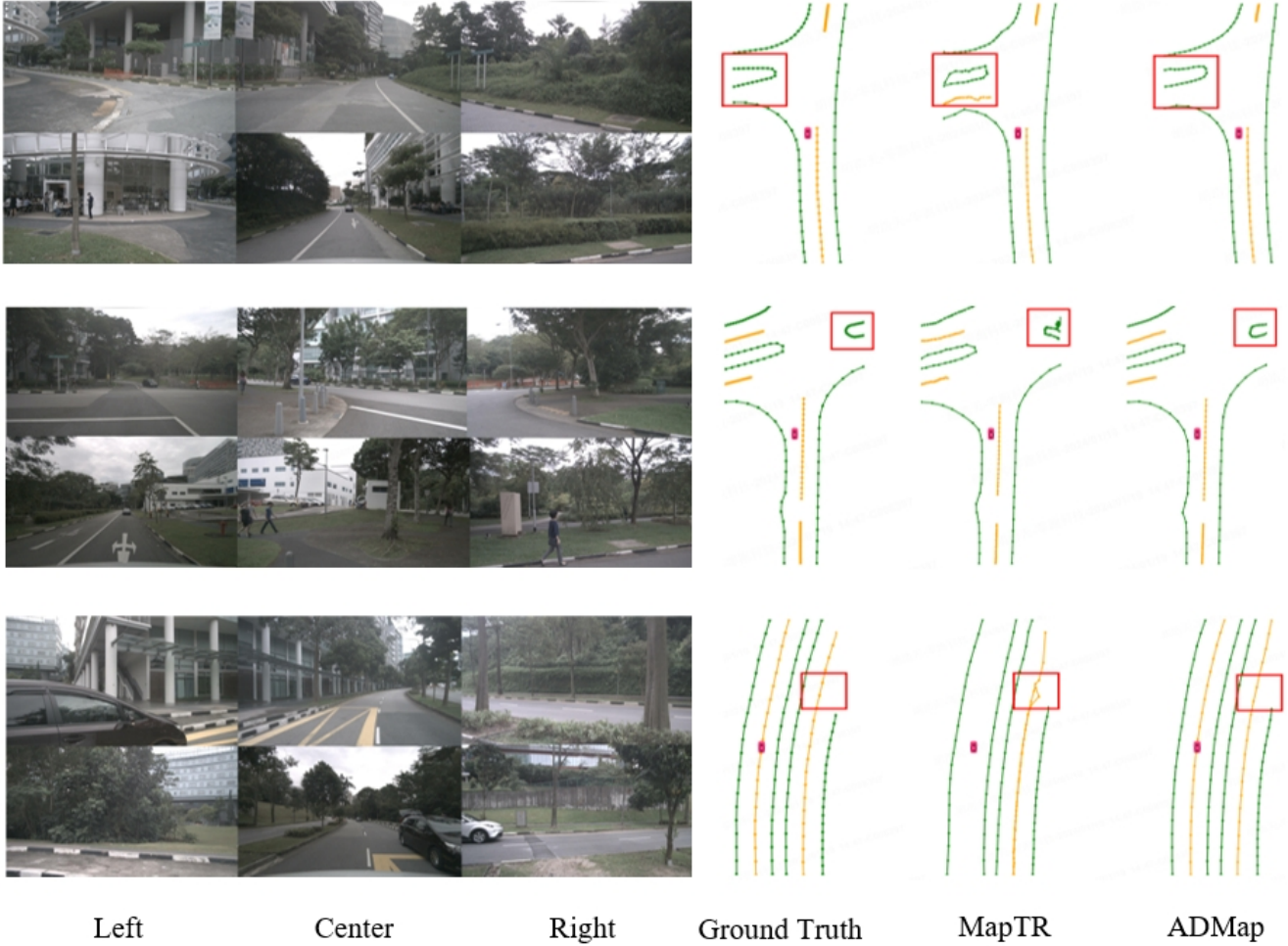


Figure 6. Visualization results of the nuScenes dataset

Table 3. Ablation experiments for each module. IIA for Instance Interactive Attention, MPN for Multi-Scale Perception Neck, and VDDL for Vector Direction Difference Loss.

Model	$AP_{div}$	$AP_{ped}$	$AP_{bou}$	mAP
MapTR baseline	62.3	56.2	69.1	62.5
+IIA	63.3	59.5	73.3	65.4
+MPN	66.0	62.9	73.6	67.3
+VDDL	<b>66.6</b>	<b>63.3</b>	<b>74.0</b>	<b>68.0</b>

Table 4. Impact of different self-attention on performance. DSA denotes Decoupled self-attention[13], IIA denotes Instance Interactive Attention.

Model	$AP_{div}$	$AP_{ped}$	$AP_{bou}$	mAP
Vanilla	62.3	56.2	69.1	62.5
+DSA	64.2	57.8	70.2	64.1
+IIA	<b>63.3</b>	<b>59.5</b>	<b>73.3</b>	<b>65.4</b>

performance is achieved when the weights are set to 1.0, with an mAP of 54.5%.

Table 7 reports the results of the ablation experiments in

Table 5. Impact of inserting the neck structure on the model performance. BackboneNeck denotes the neck structure in SECOND, MPN denotes Multi-Scale Perception Neck.

Model	$AP_{div}$	$AP_{ped}$	$AP_{bou}$	mAP
Vanilla	62.3	56.2	69.1	62.5
+BackboneNeck	62.8	58.4	70.2	63.7
+MPN	<b>65.0</b>	<b>59.6</b>	<b>69.4</b>	<b>64.5</b>

Table 6. Impact of VDDL weights on performance

Weight	$AP_{div}$	$AP_{ped}$	$AP_{bou}$	mAP
0.5	55.2	49.9	56.8	54.0
<b>1.0</b>	<b>56.2</b>	<b>49.4</b>	<b>57.9</b>	<b>54.5</b>
2.0	55.6	50.0	56.9	54.2

the nuScenes benchmark for the downsampled layers of the MPN. To balance speed and performance, we set the number of downsampling layers to 2, as increasing the number of downsampling layers can slow down model inference.

Table 7. Ablation experiments on the number of downsampled layers in MPN.

num layer	$AP_{div}$	$AP_{ped}$	$AP_{bou}$	mAP	FPS
1	66.5	68.6	74.2	69.8	6.3
2	67.9	<b>68.5</b>	74.5	70.3	<b>6.1</b>
3	<b>68.1</b>	68.3	<b>74.9</b>	<b>70.5</b>	5.2

## 4.5. Analytic

Table 8. Comparison of chamfer distance between ADMap and ADMapv2 and their respective baselines.

model	chamfer dis.
MapTR	0.597
ADMap	0.518
MapTRv2	0.560
<b>ADMapv2</b>	<b>0.422</b>

In Table 8, we calculate the average chamfer distance between all predicted instances and ground truth below the threshold (true positive instance) in the nuScenes validation set, and use it as an evaluation metric to assess the accuracy of the model in predicting instances. Smaller average chamfer distance indicates more accurate predicted instances (less instance point jitter). The chamfer distance loss of ADMap decreased by 0.079 compared to MapTR, and ADMapv2 decreased by 0.138 compared to the baseline. These results suggest that ADMap effectively mitigates the issue of inaccurate point order prediction.

## 4.6. Visualization

Table 6 shows a comparison of the visualizations between ground truth, MapTR, and ADMap in the nuscenes benchmark. The results indicate that ADMap outperforms MapTR in various scenarios. Visualizations of the Argoverse2 dataset are in the Appendix.

## 5. Conclusions

ADMap is an effective and efficient vectorized HD map reconstruction framework that effectively mitigates the problem of map topology distortion caused by instance point jitter through three modules: Multi-Scale Perception Neck, Instance Interactive Attention, and Vector Direction Difference Loss. Numerous experiments have shown that our proposed method can achieve the best performance in nuScenes and Argoverse2 benchmarks, and its high efficiency has also been verified. We believe that ADMap can assist the community in advancing research on vectorized HD map reconstruction tasks for better development in areas such as autonomous driving.

## References

- [1] Holger Caesar, Varun Bankiti, Alex H. Lang, Sourabh Vora, Venice Erin Liong, Qiang Xu, Anush Krishnan, Yu Pan, Giancarlo Baldan, and Oscar Beijbom. nuscenes: A multi-modal dataset for autonomous driving. *arXiv preprint arXiv:1903.11027*, 2019. 5
- [2] Li Chen, Chonghao Sima, Yang Li, Zehan Zheng, Jiajie Xu, Xiangwei Geng, Hongyang Li, Conghui He, Jianping Shi, Yu Qiao, and Junchi Yan. Persformer: 3d lane detection via perspective transformer and the openlane benchmark. In *European Conference on Computer Vision (ECCV)*, 2022. 2
- [3] S. Chen, T. Cheng, X. Wang, W. Meng, Q. Zhang, and W. Liu. Efficient and robust 2d-to-bev representation learning via geometry-guided kernel transformer. *arXiv preprint arXiv:2206.04584*, 2022. 1, 2
- [4] Wenjie Ding, Limeng Qiao, Xi Qiu, and Chi Zhang. Pivotnet: Vectorized pivot learning for end-to-end hd map construction. In *Proceedings of the IEEE/CVF International Conference on Computer Vision*, pages 3672–3682, 2023. 6
- [5] Noa Garnett, Rafi Cohen, Tomer Pe’er, Roei Lahav, and Dan Levi. 3d-lanenet: End-to-end 3d multiple lane detection. In *Proceedings of the IEEE/CVF International Conference on Computer Vision (ICCV)*, October 2019. 2
- [6] Yuliang Guo Guo, Guang Chen, Zhao Peitao, Zhang Weide, Jinghao Miao, Jingao Wang, and Tae Eun Choe. Genlanenet: A generalized and scalable approach for 3d lane detection. 2020. 2
- [7] Kaiming He, Xiangyu Zhang, Shaoqing Ren, and Jian Sun. Deep residual learning for image recognition. *arXiv preprint arXiv:1512.03385*, 2015. 5
- [8] A. Hu, Z. Murez, N. Mohan, S. Dudas, J. Hawke, V. Badrinarayanan, R. Cipolla, and Kendall A. Fiery: Future instance segmentation in bird’s-eye view from surround monocular cameras. *ICCV*, 2021. 1, 2
- [9] Qi Li, Yue Wang, Yilun Wang, and Hang Zhao. Hdmapnet: An online hd map construction and evaluation framework, 2021. 1, 2, 6
- [10] Z. Li, W. Wang, H. Li, E. Xie, C. Sima, T. Lu, Y. Qiao, and J. Dai. Bevformer: Learning bird’s-eye-view representation from multicamera images via spatiotemporal transformers. *ECCV*, 2022. 1, 2
- [11] Z. Li, W. Wang, H. Li, E. Xie, C. Sima, T. Lu, Y. Qiao, and J. Dai. Bevformer: Learning bird’s-eye-view representation from multicamera images via spatiotemporal transformers. *ECCV*, 2022. 2
- [12] Bencheng Liao, Shaoyu Chen, Xinggang Wang, Tianheng Cheng, Qian Zhang, Wenyu Liu, and Chang Huang. Maptr: Structured modeling and learning for online vectorized hd map construction. In *International Conference on Learning Representations*, 2023. 1, 2, 3, 6
- [13] Bencheng Liao, Shaoyu Chen, Yunchi Zhang, Bo Jiang, Qian Zhang, Wenyu Liu, Chang Huang, and Xinggang Wang. Maptrv2: An end-to-end framework for online vectorized hd map construction. *arXiv preprint arXiv:2308.05736*, 2023. 1, 3, 6, 7
- [14] Yicheng Liu, Yuan Yuantian, Yue Wang, Yilun Wang, and Hang Zhao. Vectormapnet: End-to-end vectorized hd map

- learning. In *International conference on machine learning*. PMLR, 2023. 1, 2, 6
- [15] Z. Liu, S. Chen, X. Guo, X. Wang, T. Cheng, H. Zhu, Q. Zhang, W. Liu, and Y. Zhang. Vision-based uneven bev representation learning with polar rasterization and surface estimation. *arXiv preprint arXiv:2207.01878*, 2022. 2
- [16] Davy Neven, Bert De Brabandere, Stamatios Georgoulis, Marc Proesmans, and Luc Van Gool. Towards end-to-end lane detection: an instance segmentation approach, 2018. 2
- [17] J. Phillion and S. Fidler. Lift, splat, shoot: Encoding images from arbitrary camera rigs by implicitly unprojecting to 3d. *ECCV*, 2020. 2
- [18] Limeng Qiao, Wenjie Ding, Xi Qiu, and Chi Zhang. End-to-end vectorized hd-map construction with piecewise bezier curve. In *Proceedings of the IEEE/CVF Conference on Computer Vision and Pattern Recognition (CVPR)*, pages 13218–13228, June 2023. 6
- [19] Benjamin Wilson, William Qi, Tanmay Agarwal, John Lambert, Jagjeet Singh, Siddhesh Khandelwal, Bowen Pan, Ratnesh Kumar, Andrew Hartnett, Jhony Kaesemodel Pontes, Deva Ramanan, Peter Carr, and James Hays. Argoverse 2: Next generation datasets for self-driving perception and forecasting. In *Proceedings of the Neural Information Processing Systems Track on Datasets and Benchmarks (NeurIPS Datasets and Benchmarks 2021)*, 2021. 5
- [20] Yan Yan, Yuxing Mao, and Bo Li. Second: Sparsely embedded convolutional detection. 2018. 5, 6
- [21] B. Zhou and P. Krahenbuhl. Cross-view transformers for real-time map-view semantic segmentation. *CVPR*, 2022. 1, 2